

Editor's Pick

Semi-hydro-equivalent design and performance extrapolation between 100 kJ-scale and NIF-scale indirect drive implosion

Cite as: Matter Radiat. Extremes 9, 015601 (2024); doi: 10.1063/5.0150343

Submitted: 14 March 2023 • Accepted: 22 September 2023 •

Published Online: 17 November 2023







View Online



Export Citation



CrossMark

Huasen Zhang,^{1,2}  Dongguo Kang,^{2,a)}  Changshu Wu,² Liang Hao,²  Hao Shen,² Shiyang Zou,² Shaoping Zhu,²  and Yongkun Ding²

AFFILIATIONS

¹Laboratory of Computational Physics, Institute of Applied Physics and Computational Mathematics, Beijing 10088, China²Institute of Applied Physics and Computational Mathematics, Beijing 10088, China^{a)} Author to whom correspondence should be addressed: kang_dongguo@iapcm.ac.cn

ABSTRACT

Extrapolation of implosion performance between different laser energy scales is investigated for indirect drive through a semi-hydro-equivalent design. Since radiation transport is non-hydro-equivalent, the peak radiation temperature of the hohlraum and the ablation velocity of the capsule ablator are not scale-invariant when the sizes of the hohlraum and the capsule are scale-varied. A semi-hydro-equivalent design method that keeps the implosion velocity V_i , adiabat α_F , and P_L/R_{hc}^2 (where P_L is the laser power and R_{hc} is the hohlraum and capsule scale length) scale-invariant, is proposed to create hydrodynamically similar implosions. The semi-hydro-equivalent design and the scaled implosion performance are investigated for the 100 kJ Laser Facility (100 kJ-scale) and the National Ignition Facility (NIF-scale) with about 2 MJ laser energy. It is found that the one-dimensional implosion performance is approximately hydro-equivalent when V_i and α_F are kept the same. Owing to the non-hydro-equivalent radiation transport, the yield-over-clean without α -particle heating ($YOC_{no\alpha}$) is slightly lower at 100 kJ-scale than at NIF-scale for the same scaled radiation asymmetry or the same initial perturbation of the hydrodynamic instability. The overall scaled two-dimensional implosion performance is slightly lower at 100 kJ-scale. The general Lawson criterion factor scales as $\chi_{no\alpha}^{2D} \sim S^{1.06 \pm 0.04}$ (where S is the scale-variation factor) for the semi-hydro-equivalent implosion design with a moderate $YOC_{no\alpha}$. Our study indicates that $\chi_{no\alpha} \approx 0.379$ is the minimum requirement for the 100 kJ-scale implosion to demonstrate the ability to achieve marginal ignition at NIF-scale.

© 2023 Author(s). All article content, except where otherwise noted, is licensed under a Creative Commons Attribution (CC BY) license (<http://creativecommons.org/licenses/by/4.0/>). <https://doi.org/10.1063/5.0150343>

I. INTRODUCTION

In laser-driven inertial confinement fusion (ICF),¹ a cryogenic spherical capsule filled with deuterium and tritium (DT) fuel is accelerated inward by either direct laser irradiation (direct drive)² or x rays produced by laser irradiation of a high-Z hohlraum (indirect drive).³ The compressed capsule consists of a low-density and high-temperature hotspot surrounded by a high-density and low-temperature shell. The central hotspot must achieve an extremely high-energy-density state (hundreds of Gbar) to produce significant thermonuclear reaction. Thermonuclear ignition occurs when the energy output produced by fusion reaction is much greater

than the input energy required to compress the capsule. The ignition condition is usually expressed by the Lawson criterion and can be written as $P_{hs}\tau > 10 \text{ atm s}$ for a central fuel temperature $T \approx 10 \text{ keV}$.⁴ Here, P_{hs} is the hotspot pressure at stagnation and τ is the hotspot confinement time. It is also suggested that ignition occurs for yield amplification $Y_{amp} \approx 15\text{--}30$, which corresponds to the general Lawson criterion (GLC) factor^{5–7} $\chi_{no\alpha} = 1$ or ignition threshold factor⁸ $ITFx = 1$. Here, Y_{amp} is defined as the ratio between the yield with α -particle heating (subscript α) and the yield without α -particle heating (subscript $no\alpha$) $Y_{amp} = Y_\alpha/Y_{no\alpha}$.^{9–11} The GLC factor and $ITFx$ are also used to represent the implosion performance and are approximately related by $\chi_{no\alpha} \approx ITFx^{0.34}$. In the

past few years, great progress has been made in indirect drive fusion at the National Ignition Facility (NIF).^{12–20} Indirect drive implosion with significant yield amplification has been demonstrated.^{12–16} The marginal ignition regime is reached with a fusion yield of about 1.3 MJ.^{17–19} Recently, ignition with 3.15 MJ fusion yield has been achieved at a laser energy of 2.05 MJ.²⁰

Implosions with hydrodynamic similarity can provide a way to establish an extrapolation of the implosion performance without α between different energy scales, which was first investigated for direct drive.^{21–23} Similar work is also being carried out for indirect drive to improve implosion performance at the NIF, such as scaling the capsule size from the deceleration phase,²⁶ scaling hohlraum and capsule size together,^{27,28} and scaling the capsule but not the hohlraum.^{16,27} The experimental progress at the NIF can provide valuable guidance for the indirect drive implosion experiments at the 100 kJ Laser Facility (100 kJ-scale),^{24,25} which is about one-magnitude smaller in laser energy relative to the NIF (NIF-scale). Although the implosion experiments at the 100 kJ Laser Facility are not aimed at achieving ignition owing to lack of sufficient energy, most areas of implosion physics can be investigated. To take advantage of NIF's high-performance implosion design and extrapolate the implosion performance to 100 kJ-scale, it is necessary to find a way to bridge the implosions between different laser energy scales.

In this work, extrapolation of the indirect drive implosion between 100 kJ-scale and NIF-scale is investigated numerically. Since the laser energy varies significantly between the two laser facilities, the extrapolation study is limited to the case in which the hohlraum and capsule size are scaled together. Since radiation transport is non-hydro-equivalent, a semi-hydro-equivalent design method is proposed to create hydrodynamically similar implosions between 100 kJ-scale and NIF-scale. Here, “semi-hydro-equivalent” means that the one-dimensional (1D) implosion design is close to hydro-equivalence, while the two- and three-dimensional (2D and 3D) implosion performance deviates slightly from hydro-equivalence. Instead of keeping V_i , α_F , and T_r the same for the capsule-only design, the semi-hydro-equivalent design in indirect drive keeps the values of V_i , α_F , and P_L/R_{hc}^2 the same when the hohlraum and capsule are scaled in size together. Here P_L is the laser power, and R_{hc} is the hohlraum and capsule scale length. Without loss of generality, the semi-hydro-equivalent implosion is designed for 100 kJ-scale based on NIF-scale high-performance implosion design. It is shown that the peak radiation temperature in the 100 kJ-scale hohlraum is smaller than that in the NIF-scale hohlraum for the same scaled incident laser pulse, owing to the lower x-ray conversion efficiency. The 1D implosion performance is approximately hydro-equivalent between 100 kJ-scale and NIF-scale, i.e., $\chi_{no\alpha}^{1D} \sim S^{0.95}$, with S the scale-variation factor. 2D simulations indicate that the overall scaled implosion performance is slightly lower at 100 kJ-scale owing to more significant yield degradation by the same scaled radiation asymmetry or the same initial perturbation of the hydrodynamic instability (HI). Owing to the variation of $YOC_{no\alpha}$ at different scales, it is expected that $\chi_{no\alpha}^{2D} \sim S^{1.06 \pm 0.04}$ for the semi-hydro-equivalent implosion with a moderate $YOC_{no\alpha}$. To demonstrate the ability of achieving marginal ignition in NIF-scale, the minimum $\chi_{no\alpha}^{2D} \approx 0.379$ is required for the 100 kJ-scale implosion.

The remainder of this paper is organized as follows. In Sec. II, the semi-hydro-equivalent design is discussed. In Sec. III, the 100 kJ-scale semi-hydro-equivalent design relative to NIF-scale implosion is presented and the implosion performance is compared. The implosion performance scaling and possible optimization for the 100 kJ-scale implosion are discussed in Sec. IV. Section V provides a summary. In the remainder of the paper, the implosion performance and yield are discussed without α -particle heating.

II. SEMI-HYDRO-EQUIVALENT DESIGN

In ICF, the radiation hydrodynamic equations in Lagrange coordinates can be written as

$$\frac{\partial \rho}{\partial t} + \rho \nabla \cdot \mathbf{v} = 0, \quad (1)$$

$$\rho \frac{\partial \mathbf{v}}{\partial t} + \nabla (P_e + P_i + P_r + q) = 0, \quad (2)$$

$$C_{vi} \frac{\partial T_i}{\partial t} + \left[T_i \left(\frac{\partial P_i}{\partial T_i} \right)_\rho + q \right] \frac{\partial}{\partial t} \left(\frac{1}{\rho} \right) + \frac{1}{\rho} \nabla \cdot \mathbf{F}_i = W_{ei}, \quad (3)$$

$$C_{ve} \frac{\partial T_e}{\partial t} + T_e \left(\frac{\partial P_e}{\partial T_e} \right)_\rho \frac{\partial}{\partial t} \left(\frac{1}{\rho} \right) + \frac{1}{\rho} \nabla \cdot \mathbf{F}_e = -W_{ei} - W_{er} + W_l, \quad (4)$$

$$\frac{1}{c} \frac{dI}{dt} + \boldsymbol{\Omega} \cdot \nabla I + \frac{4\rho}{3c} I \frac{\partial}{\partial t} \left(\frac{1}{\rho} \right) = W_{er}. \quad (5)$$

Here, ρ is the mass density and \mathbf{v} is the flow velocity. P is the pressure, with subscripts i , e , and r referring to ion, electron, and radiation, respectively. q is the numerical viscosity and \mathbf{F} is the thermal conduction. C_v and T are the constant-volume specific heat capacity and temperature. W_{ei} and W_{er} are the electron–ion and electron–radiation energy exchange terms, respectively. W_l represents the energy deposition of the laser, mainly through the inverse bremsstrahlung process. $I(\nu, \boldsymbol{\Omega})$ is the radiation intensity at frequency ν and direction $\boldsymbol{\Omega}$. The hydro-equivalence means that when time (t) and space (x) are varied by a scale-variation factor S , i.e., $t \rightarrow St'$, $x \rightarrow Sx'$, the intensity quantities in the equations are invariant, while the extensity quantities are scalable. In the radiation hydrodynamic equations, when the energy exchange terms (such as \mathbf{F} and W) are ignorable or hydro-equivalent, the whole system is fully hydro-equivalent. In this case, the hotspot pressure P_{hs} and hotspot ion temperature T_i are scale-invariant. The hotspot volume V scales as S^3 and the confinement time τ scales as S . The fusion yield scales as $Y_{no\alpha} \sim P_{hs}^2 T_i^2 V \tau \sim S^4$. However, owing to the non-hydro-equivalent properties of the energy exchange terms, the radiation hydrodynamic system is not fully hydro-equivalent. For example, to keep the heat flux hydro-equivalent, the thermal conduction term $\mathbf{F} = -\kappa \nabla T$ should also be $1/S$ times smaller when t and x are multiplied by S . The modification of W_{er} and W_l to maintain hydro-equivalence would be more complicated.

In Ref. 21, it was shown that implosions with the same implosion velocity V_i , adiabat α_F , and laser intensity I_L are approximately 1D hydro-equivalent. The HI growth is also approximately hydro-equivalent for the 1D hydro-equivalent design if the initial

surface perturbation is proportional to the target size. Therefore, the non-1D implosion performance due to HI degradation is also hydro-equivalent. Although it was also indicated in Ref. 21 that the hydro-equivalent implosions require the same values of V_i , α_F , and T_r for indirect drive, fully hydro-equivalent implosions are hard to achieve when the energy scale varies significantly from 100 kJ-scale to NIF-scale. One major but non-exhaustive reason is that the non-hydro-equivalent effect of the radiation transport becomes significant, which would result in the following two consequences.

1. It is hard to retain the same T_r in scale variation. In indirect drive, the radiation drive of the capsule is produced by the laser-irradiated hohlraum and satisfies the power balance equation:

$$\eta P_L = [A_w(1 - \alpha_w) + A_{LEH} + (1 - \alpha_{cap})A_{cap}] \sigma T_r^4. \quad (6)$$

Here, η is the hohlraum x-ray conversion efficiency, σ is the Stefan–Boltzmann constant, α_w and α_{cap} are the albedos of the hohlraum wall and capsule, respectively, A_w and A_{LEH} are the areas of the hohlraum wall and the laser entrance hole (LEH), respectively, and A_{cap} is the area of the capsule. When the hohlraum and capsule sizes scale together, $\eta P_L \sim [(1 - \alpha_w) + \beta] \sigma T_r^4 R_{hc}^2$, with $\beta = A_{LEH}/A_w + (1 - \alpha_{cap})A_{cap}/A_w$ depending mainly on the geometry. For a high- Z hohlraum, η and α_w increases with S .³ As a result, the peak T_r also increases with S for the same P_L/R_{hc}^2 value. To produce the same T_r as in an NIF-scale hohlraum, P_L should be higher or R_{hc} should be smaller at 100 kJ-scale. However, in indirect drive with a cylindrical hohlraum, laser plasma instability (LPI) and radiation asymmetry are coupled together and are both correlated with the laser intensity. Increasing the laser power may cause significant variation of the radiation asymmetry and the enhancement of LPI.

2. It is hard for the HI growth of the implosion to be hydro-equivalent. In indirect drive, the ablation pressure scales as $P_a \sim T_r^{3.5}$ and the mass ablation rate scales as $\dot{m}_a \sim T_r^3$. If we approximate $P_a = \alpha_{abl} \rho^{5/3}$ (α_{abl} is the adiabat of the capsule ablator) for the ablator, then the ablation velocity can be written as $v_a = \dot{m}_a/\rho_a \sim \alpha_{abl}^{3/5} T_r^{1.1}$. Because the mean free path of the x rays is comparable to the shell thickness and is scale-invariant, there is relatively more radiation preheating for the ablator in a small-scale implosion than in a large-scale one. Since α_{abl} increases with radiation preheating, the ablation velocity would be larger in a small-scale implosion than in a large-scale one for the same T_r , resulting in different ablation stabilization of the HI growth. This is different from direct drive, where the preheating of the shell by the radiation can be ignored.

Therefore, it is hard to achieve fully hydro-equivalent implosion between 100 kJ-scale and NIF-scale even when the values of V_i , α_F , and T_r are kept the same. In the semi-hydro-equivalent design, the value of P_L/R_{hc}^2 is kept the same, instead of the value of T_r . We will show below that in this case, the peak T_r is lower at 100 kJ-scale than at NIF-scale, which could partially compensate for the deviation of V_a due to different radiation preheating of the ablator. The 1D hydro-equivalent implosion quantities V_i and α_F could also be kept invariant in the semi-hydro-equivalent design. The implosion

time scales linearly with S , since $\tau_{imp} \sim R_{cap}/V_i \sim S^1$. Considering that the scale length of the hohlraum blow-off plasma bubble scales as $R_{bub} \sim C_s \tau_{imp} \sim S^1$, it is also helpful for keeping the scaled radiation asymmetry similar between 100 kJ-scale and NIF-scale, since the radiation asymmetry is mainly determined by the bubble scale in the low-filled hohlraum. Here, C_s is the sound speed of the laser-irradiated plasma, which is mainly determined by the laser intensity I_L .

In summary, when the hohlraum and capsule are scaled together in size from NIF-scale to 100 kJ-scale, the semi-hydro-equivalent design keeps the same values of V_i , α_F , and P_L/R_{hc}^2 . In this case, the implosion time scales as $\tau_{imp} \sim S^1$ and the incident laser energy scales as $E_L \sim S^3$. It is expected that the time evolution of radiation asymmetry and the HI growth will deviate less from full hydro-equivalence compared with the case with the same T_r .

III. SEMI-HYDRO-EQUIVALENT DESIGN OF 100 KJ-SCALE IMPLOSION RELATIVE TO NIF-SCALE IMPLOSION

The 100 kJ Laser Facility has 48 laser beams arranged into inner and outer cones similar to the NIF. The peak laser intensity of the laser beams in the 100 kJ Laser Facility is similar to that of the NIF. The peak power of the laser beams in the 100 kJ Laser Facility is around 1.25 TW, while that of the NIF's laser beams is around 2 TW. Therefore, the implosion scale at 100 kJ-scale is roughly 0.4 times that at the NIF-scale. In the rest of this paper, using numerical simulations, the semi-hydro-equivalent implosion design and its performances are investigated for 100 kJ-scale (denoted as S0.4) based on the NIF-scale (denoted as S1.0) high-performance implosion design. The 2D hohlraum and capsule simulations are performed using the Lagrange radiation hydrodynamic code Lared-Integration,²⁹ while the 2D capsule-only simulations are performed using the Euler radiation hydrodynamic code Lared-S.³⁰

A. 1D performance of semi-hydro-equivalent design

In this subsection, the 1D performance of the 100 kJ-scale semi-hydro-equivalent design relative to the NIF-scale high performance design is investigated. Without loss of generality, the S1.0 implosion uses the same hohlraum and capsule as the high-performance implosion N170601 at the NIF.¹² The uranium hohlraum diameter is 6.2 mm and its length is 11.3 mm. The diameter of the laser entrance hole (LEH) is 3.64 mm. The hohlraum is filled with 0.3 mg/cm³ helium. The outer radius of the capsule is 980 μ m. The capsule shell consists of 56 μ m DT ice surrounded by a 70 μ m high-density carbon (HDC) ablator. A 21 μ m HDC layer is doped with 0.3% tungsten with inner surface 7 μ m away from the DT/HDC interface. A three-shock laser pulse similar to that reported in Ref. 12 is used to drive the implosion [Fig. 1(a)]. First, the S1.0 indirect drive implosion is simulated by Lared-Integration. It is found that the peak T_r of the capsule is around 300 eV for the S1.0 implosion [black solid line in Fig. 1(b)]. When the laser pulse and hohlraum size are fully scaled down to S0.4, it is found that the scaled T_r [black dashed line in Fig. 1(b)] is overall lower than that in S1.0. This is consistent with the fact that the x-ray conversion efficiency is lower in the S0.4 hohlraum than in the S1.0 hohlraum. To keep the same α_F for the imploding fuel, the laser power of the prepulse is slightly increased for the

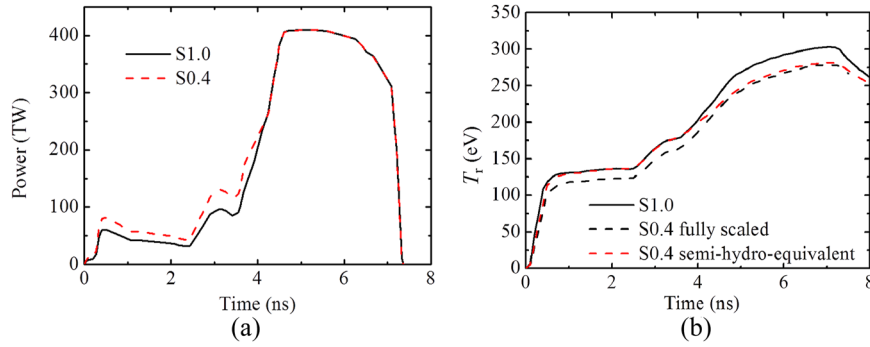


FIG. 1. Normalized laser pulse (a) and capsule radiation drive (b) for the S1.0 and the S0.4 semi-hydro-equivalent implosions. In both (a) and (b), the laser power and time of S0.4 are normalized to those of S1.0, i.e., $P_L/0.4^2$ and $t/0.4$ for S0.4.

S0.4 semi-hydro-equivalent design [red dashed line in Fig. 1(a)]. In this case, the scaled T_r before the main pulse in S0.4 is kept the same as in S1.0, while the peak T_r in S0.4 is still lower than that in S1.0 [Fig. 1(b)]. It should be noted that the slightly increasing the prepulse energy would lead to little increase in the total laser energy, which is mainly determined by the main pulse. Here, the laser backscatter by LPI is ignored, since the overall laser backscatter fraction is low for the low-gas-filled hohlraum.¹²

Table I shows comparisons of the 1D parameters and implosion performance between the S1.0 and S0.4 semi-hydro-equivalent designs. By driving the capsule with the radiation temperature of the hohlraum simulations, it is found that $\alpha_F = 2.58$ and $V_i = 383$ km/s for the S1.0 design. The no- α yield is $Y_{\text{no}\alpha} = 9.8 \times 10^{15}$. If the fully hydro-equivalent implosion could be achieved, it is to be expected that α_F , V_i , and P_{hs} in S0.4 would be the same as in S1.0. Meanwhile, $\chi_{\text{no}\alpha}^{\text{1D}}$ scales as $\chi_{\text{no}\alpha}^{\text{1D}} \sim S^{0.95}$, since $\rho R_{\text{DT}} \sim S^1$ and $Y_{\text{no}\alpha} \sim S^4$. In the S0.4 semi-hydro-equivalent design, the peak T_r is lower, mainly because of the non-hydro-equivalent radiation transport inside the

hohlraum. Since the scaled T_r before the main pulse is the same, the adiabat of the fuel can be kept the same. Meanwhile, the HDC thickness in S0.4 is slightly increased compared with the fully scaled value to create the same implosion trajectory or implosion velocity [Fig. 2(a)]. Figure 2(b) shows the density profile comparisons for the semi-hydro-equivalent design. It can be seen that the overall normalized DT shell density profiles are quite similar. The peak HDC density in S0.4 is about half of that in S1.0 because of the greater radiation preheating at the small scale. Since $v_a = \dot{m}_a/\rho_a \sim T_r^2/\rho_a$, the ablation velocity in S0.4 is about 1.6 times larger than in S1.0. Compared with the S0.4 fully hydro-equivalent results, P_{hs} and ρR_{DT} in the S0.4 semi-hydro-equivalent design are slightly smaller, owing to the lower T_r , while $Y_{\text{no}\alpha}$ is slightly larger, resulting in almost the same $\chi_{\text{no}\alpha}^{\text{1D}}$ value. Meanwhile, the scaled implosion time (neutron bangtime, nBT) is also kept the same. The simulation results indicate that when the whole target is scaled down in size from NIF-scale to 100 kJ-scale, 1D hydro-equivalence can be approximately achieved by the semi-hydro-equivalent design.

TABLE I. Comparisons of the 1D parameters and implosion performance between the S1.0 and S0.4 implosions. Here, P_{hs} and ρR_{DT} are the neutron-averaged values, which are smaller than the values at stagnation. The GLC factor is calculated by $\chi_{\text{no}\alpha}^{\text{1D}} = (0.18 Y_{\text{no}\alpha}/M_{\text{DT}})^{0.34} \rho R_{\text{DT}}^{0.61}$ according to our simulation database of the indirect drive implosion. The S1.0 and S0.4 semi-hydro-equivalent results are from simulations. The S0.4 fully hydro-equivalent results are obtained by scaling the S1.0 results to S0.4 using the classical hydro-equivalent relations.

Scale	S1.0	S0.4 full hydro-equivalence	S0.4 semi-hydro-equivalence
Peak T_r (eV)	302	302	282
HDC thickness (μm)	70	28	30
DT thickness (μm)	56	22.4	22.4
R_{in} (μm)	854	341.6	341.6
α_F	2.58	2.58	2.59
V_i (km/s)	383	383	383
nBT (ns)	8.21	3.28	3.28
P_{hs} (Gbars)	189	189	180
ρR_{DT} (g/cm^2)	0.728	0.291	0.282
$Y_{\text{no}\alpha}^{\text{1D}}$	9.8×10^{15}	2.5×10^{14}	2.7×10^{14}
$\chi_{\text{no}\alpha}^{\text{1D}}$	0.888	0.372	0.374

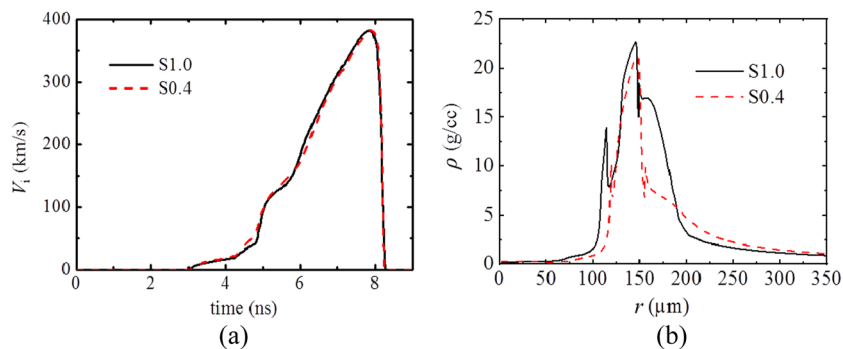


FIG. 2. Comparisons of the normalized shell velocity history (a) and the density profile at peak implosion velocity (b) for the S1.0 and S0.4 semi-hydro-equivalent implosions. In both (a) and (b), the time and space of S0.4 are normalized to those of S1.0.

B. Effects of radiation asymmetry on implosion performance

The implosion performance due to radiation asymmetry is investigated for the S1.0 and S0.4 semi-hydro-equivalent designs. Figure 3(a) shows the P2 radiation asymmetry of the capsule post-processed from the hohlraum simulations. It can be seen that the evolution of the scaled P2 radiation asymmetry is overall similar between the two semi-hydro-equivalent design. The scaled P2 radiation asymmetry of S0.4 is slightly upshifted relative to that of S1.0 around $t = 5$ ns. It should be noted that the radiation asymmetry is not optimized in the simulations. In indirect drive experiments, it has been shown that there exist ways to keep the implosion asymmetry at a low level for high-performance implosions.^{31,32} Here, we do not focus on how to tune the radiation asymmetry, but compare the implosion performance for the same scaled P2 radiation asymmetry.

We assume that the radiation asymmetry of the prepulse is well controlled and there is a small P2 radiation asymmetry during the main pulse. This assumption is reasonable since there is usually more space to control the radiation asymmetry of the prepulse. 2D capsule-only simulations were carried out using Lared-S to compare the implosion performance between the S1.0 and S0.4 semi-hydro-equivalent designs. Since there is usually a positive P2

in the late-time main pulse of the indirect drive owing to absorption of the inner cone laser by the plasma bubbles of the outer cone, two kinds of P2 radiation asymmetry are considered. In case 1, the P2 radiation asymmetry is first negative and then becomes positive during the main pulse [black line in Fig. 3(b)]. In this case, it is considered that the late-time positive P2 is significant and a negative P2 needs to be induced at early time to mitigate its impact. It is found that $\text{YOC}_{\text{no}\alpha} = 62.6\%$ for the S1.0 implosion and $\text{YOC}_{\text{no}\alpha} = 54.5\%$ for the S0.4 implosion. In case 2, the P2 radiation asymmetry is well controlled and only a small positive P2 exists in the late-time main pulse [red line in Fig. 3(b)]. It is found that $\text{YOC}_{\text{no}\alpha} = 83.5\%$ for the S1.0 implosion and $\text{YOC}_{\text{no}\alpha} = 71.1\%$ for the S0.4 implosion. Both cases show that $\text{YOC}_{\text{no}\alpha}$ in S0.4 is slightly lower than that in S1.0. Figure 4 compares the shell density at nBT between the S1.0 and S0.4 implosions. It is found that the inner surface in S0.4 is slightly more deviated from 1D than that in S1.0, which results in the lower $\text{YOC}_{\text{no}\alpha}$ in S0.4 relative to that in S1.0. The non-hydro-equivalence of the shell shape is probably because the larger ablation velocity in S0.4 results in less scaled remaining mass and causes more variation of the implosion velocity in the polar direction. The simulation results indicate that the larger-scale semi-hydro-equivalent implosion is more tolerant of radiation asymmetry and has a higher $\text{YOC}_{\text{no}\alpha}$ under the same scaled radiation asymmetry.

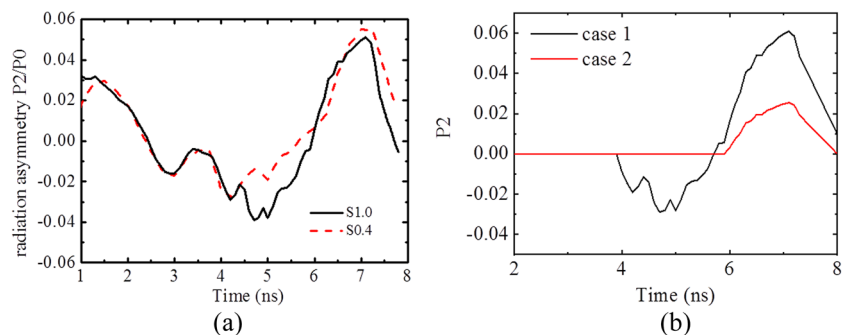


FIG. 3. (a) Comparison of normalized P2 radiation asymmetry for the S1.0 and S0.4 hohlraums. (b) Normalized P2 radiation asymmetry used for the semi-hydro-equivalent implosions. The time of S0.4 is normalized to that of S1.0.

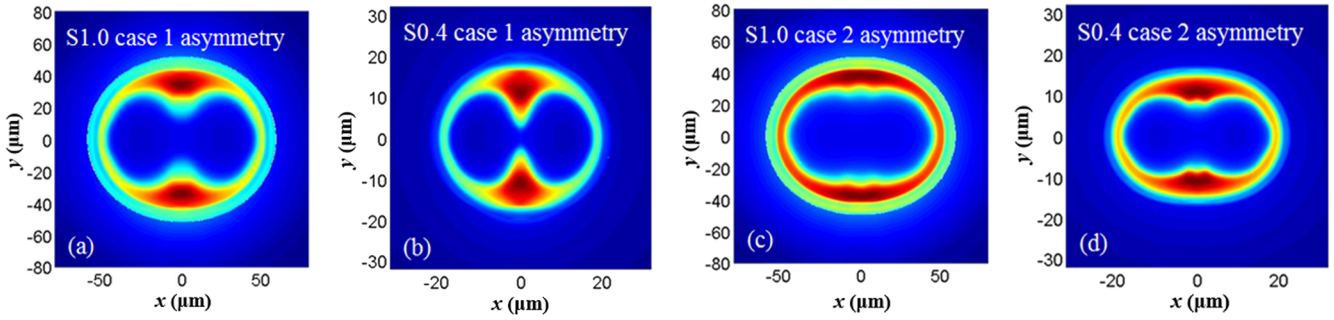


FIG. 4. Comparisons of shell density at nBT for the same scaled P2 radiation asymmetry.

C. Effects of hydrodynamic instability on implosion performance

The Rayleigh–Taylor instability (RTI)^{33,34} and Richtmyer–Meshkov instability (RMI)^{35,36} are the major HIs that degrade implosion performance. If the imploding capsule is fully hydro-equivalent, then the HI growth and the correlated $YOC_{no\alpha}$ should be scale-invariant. For semi-hydro-equivalent implosion, the ablation velocity and the Atwood number at the ablation front vary with scales, which will result in variation of HI growth and the correlated $YOC_{no\alpha}$. Here, we take RTI as an example to discuss HI growth in semi-hydro-equivalent implosions. In the linear regime, the growth rate of the ablative RTI can be approximately described by Takabe’s formula:³⁷ $\gamma = \sqrt{A_T k g} - b k V_a$, where A_T is the Atwood number, g is the acceleration rate, and $k = L/R$ is the wavenumber, with L the mode number. The coefficient $b = 3-4$ in the regime of interest. The bubble front growth factor (GF), defined as the bubble amplitude h_b divided by the initial perturbation amplitude h_0 , satisfies $GF = h_b/h_0 = \exp(\int \gamma dt)$. In the nonlinear regime, the growth of h_b follows an $\alpha_b g t^2$ scaling law, with α_b given by ablative bubble competition theory as³⁸⁻⁴⁰

$$\alpha_b = \frac{(1 - b\sqrt{k_0/gV_a})C\sqrt{\pi}}{4} \left(\ln \frac{2C\sqrt{\pi}}{k_0 h_0} - 1 \right)^{-1}. \quad (7)$$

Here, $C \approx 0.56$ for 2D and $C \approx 0.9$ for 3D. By following a similar derivation to that in Sec. II of Ref. 21, it is found that $h_b/\Delta_a \sim 2\alpha_b(R_0 - R_a)/\Delta_a$, where R_0 is the initial shell radius, and R_a and Δ_a are the shell radius and shell thickness at the end of the acceleration. In a semi-hydro-equivalent implosion, the values of Δ_a/Δ_0 and $(R_0 - R_a)/\Delta_a$ are roughly scale-invariant (Fig. 2). Therefore, $h_b/\Delta_a \sim GF \cdot h_0/\Delta_0$ in the linear limit and $h_b/\Delta_a \sim \alpha_b$ in the nonlinear limit. We further assume that the RTI initial seeds are mainly from capsule surface perturbations, such as surface roughness or defects. It is more reasonable to consider that the initial perturbation is scale-invariant rather than scale-variant. In the linear limit, h_0/Δ_0 is larger in S0.4, while GF is smaller owing to the larger V_a . It is hard to determine whether h_b/Δ_a is smaller or larger in the S0.4 implosion. Meanwhile, nonlinear theory indicates that h_b/Δ_a is smaller in the S0.4 implosion owing to the larger V_a . Considering that high-performance implosions are usually designed away from the fully nonlinear HI regime, it is not clear whether the final implosion performance is more affected by the initial perturbation amplitude h_0 or the ablation stabilization. In the rest of this subsection, the effect of scale-invariant HI perturbations on implosion performance is investigated for the semi-hydro-equivalent design using 2D capsule-only simulations. The effect of scale-variant perturbations on implosion performance is only considered when interpreting the simulation results.

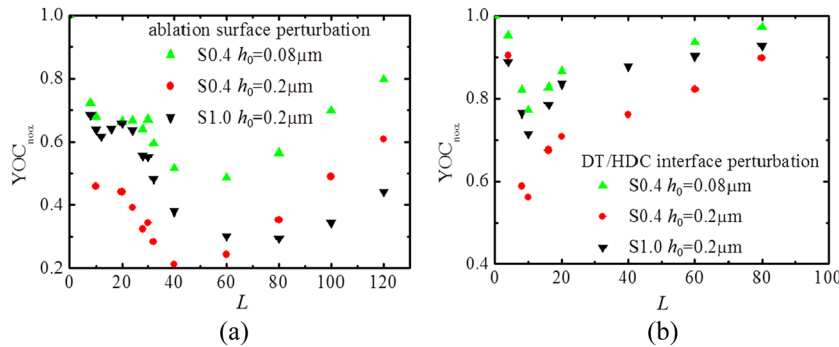

 FIG. 5. $YOC_{no\alpha}$ vs single mode-perturbation of the ablation surface (a) and the DT/HDC interface (b) for semi-hydro-equivalent implosions.

Figure 5 shows the dependence of $YOC_{no\alpha}$ on single-mode perturbation. In the S1.0 simulations, $h_0 = 0.2 \mu\text{m}$ is used for all the single modes. The S0.4 simulations with $h_0 = 0.2 \mu\text{m}$ correspond to the cases in which the initial perturbation is scale-invariant, while the S0.4 simulations with $h_0 = 0.08 \mu\text{m}$ correspond to the cases in which the initial perturbation is proportional to the capsule size. In the S1.0 simulations with ablation surface perturbation [Fig. 5(a)], it is found that $YOC_{no\alpha}$ decreases with increasing L at $L < 60$ and increases with increasing L at $L > 60$. The dependence of $YOC_{no\alpha}$ on L is consistent with the dependence of the ablative RTI growth rate on L , which increases with increasing L at small L and decreases with increasing L at large L . In the S0.4 simulations with $h_0 = 0.08 \mu\text{m}$, $YOC_{no\alpha}$ is close to that in the S1.0 simulations at $L < 20$. In this regime, the effect of ablation on stabilizing HI growth is weak. The HI growth tends to hydro-equivalence for the semi-hydro-equivalent design, resulting in almost the same $YOC_{no\alpha}$ for the S0.4 and S1.0 simulations. In the $L > 20$ regime, $YOC_{no\alpha}$ in the S0.4 simulations with $h_0 = 0.08 \mu\text{m}$ is higher than that in the S1.0 simulations. The deviation of $YOC_{no\alpha}$ increases with increasing L . This is consistent with the facts that the ablation velocity is larger in the S0.4 implosion and the ablation stabilization is more significant for small-scale perturbations. Therefore, $YOC_{no\alpha}$ in S0.4 will be higher than that in S1.0 if the HI initial perturbation scales with capsule size. In the S0.4 simulations with $h_0 = 0.2 \mu\text{m}$, $YOC_{no\alpha}$ is overall about 20% downshifted compared with the S0.4 simulations with $h_0 = 0.08 \mu\text{m}$. The minimum $YOC_{no\alpha}$ in the S0.4 simulations with $h_0 = 0.2 \mu\text{m}$ is lower than that in the S1.0 simulations, indicating that the initial perturbation amplitude is more dominant in determining the performance than ablation stabilization. In the simulations with interface perturbation [Fig. 5(b)], $YOC_{no\alpha}$ in the S1.0 simulations with $h_0 = 0.2 \mu\text{m}$ is close to that in the S0.4 simulations with $h_0 = 0.08 \mu\text{m}$ and is higher than that in the S0.4 simulations with $h_0 = 0.2 \mu\text{m}$ for all modes. It should be noted that the interface is hydrodynamically stable in the early-time acceleration phase, because the density of the ablator is higher than that of the DT ice at early times. The interface perturbation could feed through to the ablation front and induce the ablative RTI growth. The HI growth of the ablation front would feed back to the interface and enlarge its perturbation. Owing to the radiation preheating of the ablator, the density of the ablator becomes lower than that of the DT ice in the late-time acceleration phase, and the interface will also become hydrodynamically unstable. The interface HI growth is close to the classical case, since ablation stabilization has little effect on it. Owing to the more significant radiation preheating of the ablator, the Atwood number of the interface reverses earlier and is larger in the S0.4 simulation than the S1.0 simulation in the late-time acceleration phase [Fig. 2(b)]. It can be expected that the interface HI growth will be more significant in the S0.4 simulation than the S1.0 simulation. Overall, the interface HI growth is quite complex. The simulation results indicate that $YOC_{no\alpha}$ is almost the same when h_0 scales with size, while $YOC_{no\alpha}$ is lower at the small scale when h_0 is scale-invariant for the interface perturbation.

Performance degradation by multimode perturbation is also investigated for semi-hydro-equivalent implosions. Perturbations with mode number $L = 6-80$ is initially induced in the simulations. Figure 6 show the initial perturbation spectrum. The overall perturbation amplitude is denoted by $\sigma = 1.0$. Table II shows comparisons of $YOC_{no\alpha}$ for the semi-hydro-equivalent implosions when the

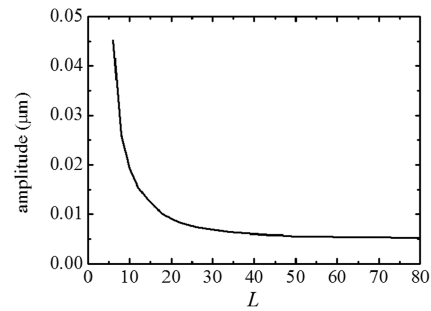


FIG. 6. Initial perturbation spectrum in the multimode simulations.

TABLE II. Comparisons of $YOC_{no\alpha}$ for semi-hydro-equivalent implosions.

Perturbation mode:	Ablation surface (%)		Interface (%)
	$L = 6-80$	$L = 6-24$	$L = 6-80$
S1.0, $\sigma = 1.0$	72.0	86.9	91.5
S0.4, $\sigma = 1.0$	59.0	65.2	82.3
S0.4, $\sigma = 0.4$	84.6	88.0	94.8

perturbation is initialized on the ablation surface and the interface, respectively. It is found that $YOC_{no\alpha}$ in the S0.4 simulations with $\sigma = 0.4$ is slightly higher than that in the S1.0 simulations, while $YOC_{no\alpha}$ in the S0.4 simulations with $\sigma = 1.0$ is about 10% lower. These results are qualitatively consistent with the single-mode simulations, indicating that the initial perturbation amplitude is more dominant in determining implosion performance. Furthermore, the $YOC_{no\alpha}$ values of the two scaled implosions are close when only the $L = 6-24$ modes are induced and the amplitude scales with size (Table II). These results recover the hydro-equivalent limit for the semi-hydro-equivalent design if ablation stabilization is unimportant and the initial perturbation amplitude scales with size.

Figure 7 shows comparisons of the shell density at nBT for the multimode simulations. In the ablation surface perturbation cases, the shell inner surface is less perturbed in the S0.4 simulation with $\sigma = 0.4$ than that in the S1.0 simulation with $\sigma = 1.0$. In the interface perturbation cases, the shell inner surface is similar between the S0.4 simulation with $\sigma = 0.4$ and the S1.0 simulation with $\sigma = 1.0$. The shell inner surface is perturbed mostly in the S0.4 simulations with $\sigma = 1.0$ for both ablation surface and interface perturbations. The multimode simulations also show that $YOC_{no\alpha}$ in S0.4 is about 10% lower than that in S1.0 when h_0 is scale-invariant.

It should be noted that the investigation of performance degradation by HI growth is based on 2D simulations. However, realistic HI perturbation seeds are usually 3D, such as surface roughness, filling tube, and supporting membranes. In the case of RTI growth, for example, a 3D perturbation has the same HI growth as a 2D perturbation in the linear regime. In the nonlinear regime, both 2D and 3D RTI follow the same scaling law [Eq. (7)], with α_b being larger in 3D for the same initial perturbation and ablation velocity.⁴⁰ It can be

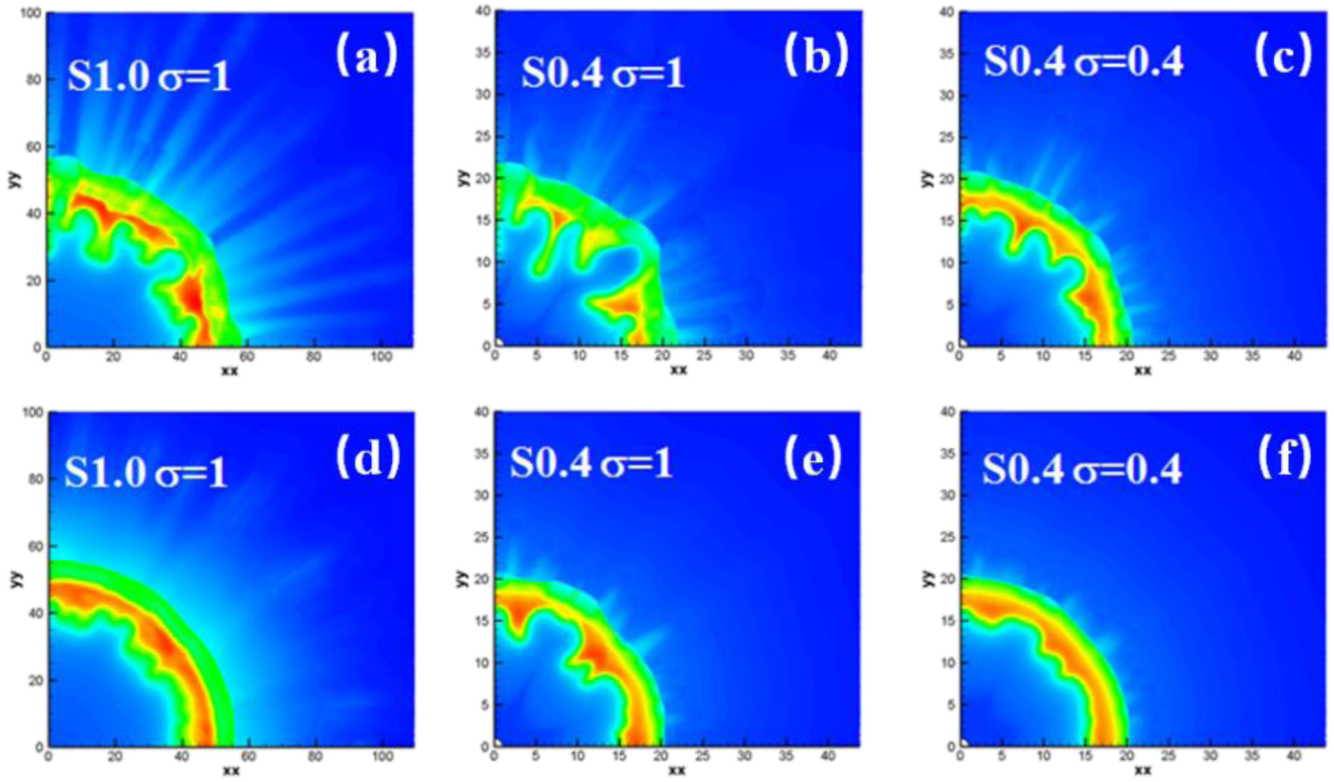


FIG. 7. Comparisons of shell density at nBT for multimode simulations with (a)–(c) ablation surface perturbation and (d)–(f) interface perturbation.

expected that $YOC_{no\alpha}$ in S0.4 will still be lower than in S1.0. Quantitative assessment of the effect of 3D perturbations in degrading implosion performance requires 3D simulations.

IV. DISCUSSION OF IMPLOSION PERFORMANCE SCALING AND POSSIBLE OPTIMIZATION FOR S0.4 IMPLOSION

In this section, the overall performance and a possible optimization strategy for the semi-hydro-equivalent design are dis-

cussed based on the simulation results. The detailed implosion performance is compared in Table III. It is found that the scaled $\chi_{no\alpha}^{1D}$ can be kept almost the same in the semi-hydro-equivalent design when the whole target size is scaled down from NIF-scale (S1.0) to 100 kJ-scale (S0.4). In this case, $\chi_{no\alpha}^{1D}$ scales as $\chi_{no\alpha}^{1D} \sim S^{0.95}$ and $Y_{no\alpha}^{1D}$ scales as $Y_{no\alpha}^{1D} \sim S^{3.92}$. It is also found that $YOC_{no\alpha}$ in S0.4 is roughly 10% lower than that in S1.0 when the scaled radiation asymmetry is the same or the capsule initial perturbation is the same. For simplicity, we assume that the radiation asymmetry can be controlled

TABLE III. Comparisons of implosion performance between different design strategies. The 2D GLC factor is calculated by $\chi_{no\alpha}^{2D} = \chi_{no\alpha}^{1D} YOC_{no\alpha}^{\mu}$ with $\mu = 0.5$ based on our simulation database of indirect drive implosions.

Scale	S1.0	S0.4 full hydro-equivalence	S0.4 semi-hydro-equivalence	S0.4 lower V_i	S0.4 higher α_F
α_F	2.58	2.58	2.59	2.60	3.4
V_i (km/s)	383	383	383	353	394
P_{hs} (Gbars)	189	189	180	153	169
ρR_{DT} (g/cm ²)	0.728	0.291	0.282	0.277	0.258
$Y_{no\alpha}^{1D}$	9.8×10^{15}	2.5×10^{14}	2.7×10^{14}	1.4×10^{14}	2.6×10^{14}
$\chi_{no\alpha}^{1D}$	0.888	0.372	0.374	0.299	0.351
YOC_{abl} (%)	72	72	59	72	64
$Y_{no\alpha}^{2D}$	7.1×10^{15}	1.8×10^{14}	1.6×10^{14}	1.0×10^{14}	1.7×10^{14}
$\chi_{no\alpha}^{2D}$	0.754	0.316	0.287	0.254	0.281

well and that the yield degradation is mainly from the perturbation on the ablation surface. In this case, $YOC_{no\alpha} \approx 72\%$ for the S1.0 implosion and $YOC_{no\alpha} \approx 59\%$ for the S0.4 implosion, indicating that $YOC_{no\alpha} \sim S^{0.22}$ if there exists a scaling law. Therefore, $\chi_{no\alpha}^{2D}$ scales as $\chi_{no\alpha}^{2D} \sim \chi_{no\alpha}^{1D} YOC_{no\alpha}^{0.5} \sim S^{1.05}$ and $Y_{no\alpha}^{2D}$ scales as $Y_{no\alpha}^{2D} \sim Y_{no\alpha}^{1D} YOC_{no\alpha}^{0.5} \sim S^{4.14}$. If we consider that $YOC_{no\alpha}$ at 100 kJ-scale is roughly 10% lower than that at NIF-scale for the semi-hydro-equivalent design, it is expected that $\chi_{no\alpha}^{2D} \sim S^{1.03-1.1}$ when the NIF-scale implosion has a moderate $YOC_{no\alpha}$, i.e., $YOC_{no\alpha} \approx 40\%-70\%$. Therefore, $\chi_{no\alpha}^{2D} \sim S^{1.06 \pm 0.04}$ for the semi-hydro-equivalent design. The scaling law of the GLC factor and the yield for the semi-hydro-equivalent design can provide a goal for the 100 kJ-scale implosion experiments with reference to the implosion experiments at NIF-scale. For example, we assume that marginal ignition is achieved for the NIF-scale implosion with yield ~ 1 MJ and $Y_{amp} = 30$. In this case, $\chi_{no\alpha} \approx 1$ and $Y_{no\alpha} \approx 1.2 \times 10^{16}$ for the S1.0 implosion. Applying the scaling law for the semi-hydro-equivalent design, it is found that a minimum $\chi_{no\alpha} \approx 0.379$ is required for the 100 kJ-scale implosion with moderate $YOC_{no\alpha}$ to demonstrate the ability to achieve marginal ignition at NIF-scale. Since the yield amplification $Y_{amp} \approx 1.3$ is not significant for $\chi_{no\alpha} \approx 0.379$, the correlated neutron yield is about $Y_{\alpha} \approx 3 \times 10^{14}$ for the 100 kJ-scale implosion.

Since NIF-scale high performance implosions are usually designed close to the HI cliff to pursue high enough implosion velocity,²⁷ it is possible that the implosion performance may decrease significantly for the S0.4 semi-hydro-equivalent implosion if the perturbation exceeds the HI cliff. Here, we discuss two possible but non-exhaustive optimizing strategies to avoid the HI cliff for the S0.4 implosion. The first strategy is to use lower V_i and the second one is to use higher α_F . Table III also shows comparisons of the implosion performance for the S0.4 implosion with different optimizing strategies. In the lower- V_i design, the HDC thickness is slightly increased while other parameters remain unchanged. In the higher- α_F design, both the prepulse and the HDC thickness are slightly changed. The $YOC_{no\alpha}^{2D}$ is obtained by multimode simulations with the $\sigma = 1.0$ ablation surface perturbation (Fig. 6). In the lower- V_i case, V_i is reduced to 353 km/s to achieve the same $YOC_{no\alpha}^{2D}$ as in the S1.0 implosion. However, $\chi_{no\alpha}^{1D}$ is significantly reduced by the lower V_i , resulting in overall much lower $\chi_{no\alpha}^{2D}$. Meanwhile, a longer implosion time is required for the low-velocity implosion, which would increase the difficulty of tuning the radiation asymmetry. In the higher- α_F case, $YOC_{no\alpha}$ is higher while $\chi_{no\alpha}^{1D}$ is lower relative to the S0.4 semi-hydro-equivalent design, resulting in less reduction of $\chi_{no\alpha}^{2D}$ than for the lower- V_i design. There may be some space for the higher- α_F design to produce better performance implosion than the semi-hydro-equivalent design. Therefore, it may be better to use the higher- α_F design to optimizing the S0.4 semi-hydro-equivalent implosion.

V. SUMMARY

A semi-hydro-equivalent design method has been proposed to establish a way to extrapolate implosion performance between different energy scales in indirect drive. Owing to the non-hydro-equivalent properties of radiation transport, the semi-hydro-equivalent design keeps the values of V_i , α_F , and P_L/R_{hc}^2 the same when the hohlraum and capsule are scaled in size together. The

semi-hydro-equivalent implosion at 100 kJ-scale is designed based on the NIF-scale high-performance implosion design. The scaled implosion performance has also been compared by numerical simulations. It is found that the peak T_r at 100 kJ-scale is smaller than that at NIF-scale, owing to the lower x-ray conversion efficiency and that the time-dependent radiation asymmetries are approximately similar. The 1D implosion performance is nearly hydro-equivalent when V_i and α_F are kept the same. 2D simulations with the same scaled radiation asymmetry show that $YOC_{no\alpha}$ at 100 kJ-scale is about 10% lower than that at NIF-scale. Because the initial perturbation amplitude of the HI is more significant than ablation stabilization in determining yield degradation, $YOC_{no\alpha}$ at 100 kJ-scale is also about 10% lower than that at NIF-scale when the initial perturbation amplitude is the same. Our study indicates that $\chi_{no\alpha} \approx 0.379$ can be regarded as a reasonable goal for the 100 kJ Laser Facility to pursue ignition in an NIF-scale laser facility.

ACKNOWLEDGMENTS

This research was funded by the National Natural Science Foundation of China (NSFC) under Grant No. 11975056 and Science Challenge Project (SCP) No. TZ2016005.

AUTHOR DECLARATIONS

Conflict of Interest

The authors have no conflicts to disclose.

Author Contributions

Huasen Zhang: Conceptualization (lead); Data curation (lead); Formal analysis (lead); Investigation (lead); Methodology (lead); Resources (lead); Writing – original draft (lead); Writing – review & editing (lead). **Dongguo Kang:** Conceptualization (supporting); Investigation (supporting); Methodology (supporting); Resources (supporting); Writing – review & editing (supporting). **Changshu Wu:** Investigation (supporting); Resources (supporting). **Liang Hao:** Investigation (supporting); Resources (supporting). **Hao Shen:** Investigation (supporting); Resources (supporting). **Shiyang Zou:** Conceptualization (supporting); Project administration (supporting); Resources (supporting). **Shaoping Zhu:** Funding acquisition (equal); Project administration (supporting); Resources (supporting). **Yongkun Ding:** Project administration (supporting); Resources (supporting).

DATA AVAILABILITY

The data that support the findings of this study are available from the corresponding author upon reasonable request.

REFERENCES

- S. Atzeni and J. Meyer-ter-Vehn, *The Physics of Inertial Fusion* (Clarendon, Oxford, 2004).
- R. S. Craxton, K. S. Anderson, T. R. Boehly, V. N. Goncharov, D. R. Harding *et al.*, “Direct-drive inertial confinement fusion: A review,” *Phys. Plasmas* **22**, 110501 (2015).

- ³J. D. Lindl, P. Amendt, R. L. Berger, S. G. Glendinning, S. H. Glenzer *et al.*, “The physics basis for ignition using indirect-drive targets on the National Ignition Facility,” *Phys. Plasmas* **11**, 339 (2004).
- ⁴J. D. Lawson, “Some criteria for a power producing thermonuclear reactor,” *Proc. Phys. Soc., London, Sect. B* **70**, 6 (1957).
- ⁵C. D. Zhou and R. Betti, “A measurable Lawson criterion and hydro-equivalent curves for inertial confinement fusion,” *Phys. Plasmas* **15**, 102707 (2008).
- ⁶P. Y. Chang, R. Betti, B. K. Spears, K. S. Anderson, J. Edwards *et al.*, “Generalized measurable ignition criterion for inertial confinement fusion,” *Phys. Rev. Lett.* **104**, 135002 (2010).
- ⁷R. Betti, P. Y. Chang, B. K. Spears, K. S. Anderson, J. Edwards *et al.*, “Thermonuclear ignition in inertial confinement fusion and comparison with magnetic confinement,” *Phys. Plasmas* **17**, 058102 (2010).
- ⁸B. K. Spears, S. Glenzer, M. J. Edwards, S. Brandon, D. Clark *et al.*, “Performance metrics for inertial confinement fusion implosions: Aspects of the technical framework for measuring progress in the National Ignition Campaign,” *Phys. Plasmas* **19**, 056316 (2012).
- ⁹J. D. Lindl, O. Landen, J. Edwards, E. Moses, and NIC Team, “Review of the National Ignition Campaign 2009-2012,” *Phys. Plasmas* **21**, 020501 (2014).
- ¹⁰A. R. Christopherson, R. Betti, J. Howard, K. M. Woo, A. Bose *et al.*, “Theory of alpha heating in inertial fusion: Alpha-heating metrics and the onset of the burning-plasma regime,” *Phys. Plasmas* **25**, 072704 (2018).
- ¹¹J. D. Lindl, S. W. Haan, O. L. Landen, A. R. Christopherson, and R. Betti, “Progress toward a self-consistent set of 1D ignition capsule metrics in ICF,” *Phys. Plasmas* **25**, 122704 (2018).
- ¹²S. Le Pape, L. F. Berzak Hopkins, L. Divol, A. Pak, E. Dewald, “Fusion energy output greater than the kinetic energy of an imploding shell at the National Ignition Facility,” *Phys. Rev. Lett.* **120**, 245003 (2018).
- ¹³P. K. Patel, P. T. Springer, C. R. Weber, L. C. Jarrott, O. A. Hurricane *et al.*, “Hotspot conditions achieved in inertial confinement fusion experiments on the National Ignition Facility,” *Phys. Plasmas* **27**, 050901 (2020).
- ¹⁴A. B. Zylstra, A. L. Kritcher, O. A. Hurricane, D. A. Callahan, K. Baker *et al.*, “Record energetics for an inertial fusion implosion at NIF,” *Phys. Rev. Lett.* **126**, 025001 (2021).
- ¹⁵A. B. Zylstra, O. A. Hurricane, D. A. Callahan, A. L. Kritcher, J. E. Ralph *et al.*, “Burning plasma achieved in inertial fusion,” *Nature* **601**, 542 (2022).
- ¹⁶A. L. Kritcher, C. V. Young, H. F. Robey, C. R. Weber, A. B. Zylstra *et al.*, “Design of inertial fusion implosions reaching the burning plasma regime,” *Nat. Phys.* **18**, 251 (2022).
- ¹⁷H. Abu-Shawareb, R. Acree, P. Adams, J. Adams, B. Addis, “Lawson criterion for ignition exceeded in an inertial fusion experiment,” *Phys. Rev. Lett.* **129**, 075001 (2022).
- ¹⁸A. L. Kritcher, A. B. Zylstra, D. A. Callahan, O. A. Hurricane, C. R. Weber *et al.*, “Design of an inertial fusion experiment exceeding the Lawson criterion for ignition,” *Phys. Rev. E* **106**, 025201 (2022).
- ¹⁹A. B. Zylstra, A. L. Kritcher, O. A. Hurricane, D. A. Callahan, J. E. Ralph *et al.*, “Experimental achievement and signatures of ignition at the National Ignition Facility,” *Phys. Rev. E* **106**, 025202 (2022).
- ²⁰B. Bishop, National Ignition Facility Achieves Fusion Ignition, December 14, 2022; <http://www.llnl.gov/news/national-ignition-facility-achieves-fusion-ignition>.
- ²¹R. Nora, R. Betti, K. S. Anderson, A. Shvydlyk, A. Bose *et al.*, “Theory of hydro-equivalent ignition for inertial fusion and its applications to OMEGA and the National Ignition Facility,” *Phys. Plasmas* **21**, 056316 (2014).
- ²²A. Bose, K. M. Woo, R. Betti, E. M. Campbell, D. Mangino *et al.*, “Core conditions for alpha heating attained in direct-drive inertial confinement fusion,” *Phys. Rev. E* **94**, 011201(R) (2016).
- ²³A. Bose, R. Betti, D. Mangino, K. M. Woo, D. Patel *et al.*, “Analysis of trends in experimental observables: Reconstruction of the implosion dynamics and implications for fusion yield extrapolation for direct-drive cryogenic targets on OMEGA,” *Phys. Plasmas* **25**, 062701 (2018).
- ²⁴X. T. He and W. Y. Zhang, “Inertial fusion research in China,” *Eur. Phys. J. D* **44**, 227 (2007).
- ²⁵W. Zheng, X. Wei, Q. Zhu, F. Jing, D. Hu *et al.*, “Laser performance of the SG-III laser facility,” *High Power Laser Sci. Eng.* **4**, e21 (2016).
- ²⁶D. S. Clark, C. R. Weber, J. L. Milovich, A. E. Pak, D. T. Casey, B. A. Hammel, D. Ho, O. S. Jones, J. M. Koning, A. L. Kritcher *et al.*, “Three-dimensional modeling and hydrodynamic scaling of National Ignition Facility implosions,” *Phys. Plasmas* **26**, 050601 (2019).
- ²⁷O. A. Hurricane, P. T. Springer, P. K. Patel, D. A. Callahan, K. Baker *et al.*, “Approaching a burning plasma on the NIF,” *Phys. Plasmas* **26**, 052704 (2019).
- ²⁸A. B. Zylstra, D. T. Casey, A. Kritcher, L. Pickworth, B. Bachmann *et al.*, “Hot-spot mix in large-scale HDC implosions at NIF,” *Phys. Plasmas* **27**, 092709 (2020).
- ²⁹P. Song, C. L. Zhai, S. G. Li, H. Yong, J. Qi, X. D. Hang, R. Yang, J. Cheng, Q. H. Zeng, X. Y. Hu, S. Wang, Y. Shi, W. D. Zheng, P. J. Gu, S. Y. Zou, X. Li, Y. Q. Zhao, H. S. Zhang, A. Q. Zhang, H. B. An, J. H. Li, W. B. Pei, and S. P. Zhu, “LARED-Integration code for numerical simulation of the whole process of the indirect-drive laser inertial confinement fusion,” *High Power Laser Part. Beams* **27**, 032007 (2015).
- ³⁰Z. Fan, X. T. He, J. Liu, G. Ren, B. Liu, J. Wu, L. F. Wang, and W. Ye, “A wedged-peak-pulse design with medium fuel adiabat for indirect-drive fusion,” *Phys. Plasmas* **21**, 100705 (2014).
- ³¹S. A. MacLaren, L. P. Masse, C. E. Czajka, S. F. Khan, G. A. Kyrala *et al.*, “A near one-dimensional indirectly driven implosion at convergence ratio 30,” *Phys. Plasmas* **25**, 056311 (2018).
- ³²D. A. Callahan, O. A. Hurricane, J. E. Ralph, C. A. Thomas, K. L. Baker *et al.*, “Exploring the limits of case-to-capsule ratio, pulse length, and picket energy for symmetric hohlraum drive on the National Ignition Facility Laser,” *Phys. Plasmas* **25**, 056305 (2018).
- ³³Lord Rayleigh, “Investigation of the character of the equilibrium of an incompressible heavy fluid of variable density,” *Proc. London Math. Soc.* **s1-14**, 170 (1882).
- ³⁴G. Taylor, “The instability of liquid surface when accelerated in a direction perpendicular to their planes,” *Proc. R. Soc. London, Ser. A* **201**, 192 (1950).
- ³⁵R. D. Richtmyer, “Taylor instability in shock acceleration of compressible fluid,” *Commun. Pure Appl. Math.* **13**, 297 (1960).
- ³⁶E. E. Meshkov, “Instability of the interface of two gases accelerated by a shock wave,” *Fluid Dyn* **4**, 101 (1969).
- ³⁷H. Takabe, K. Mima, L. Montierth, and R. L. Morse, “Self-consistent growth rate of the Rayleigh–Taylor instability in an ablatively accelerating plasma,” *Phys. Fluids* **28**, 3676 (1985).
- ³⁸H. Zhang, R. Betti, V. Gopalaswamy, R. Yan, and H. Aluie, “Nonlinear excitation of the ablatively Rayleigh–Taylor instability for all wave numbers,” *Phys. Rev. E* **97**, 011203(R) (2018).
- ³⁹H. Zhang, R. Betti, R. Yan, and H. Aluie, “Nonlinear bubble competition of the multimode ablatively Rayleigh–Taylor instability and applications to inertial confinement fusion,” *Phys. Plasmas* **27**, 122701 (2020).
- ⁴⁰H. Zhang, R. Betti, R. Yan, D. Zhao, D. Shvarts, and H. Aluie, “Self-similar multimode bubble-front evolution of the ablatively Rayleigh–Taylor instability in two and three dimensions,” *Phys. Rev. Lett.* **121**, 185002 (2018).